THERMODYNAMICS

Variance sum rule for entropy production

I. Di Terlizzi[1,2]†, M. Gironella[3,4]†, D. Herraez-Aguilar[5], T. Betz[6,7], F. Monroy[8,9], M. Baiesi[2,10], F. Ritort[3,11]*

Entropy production is the hallmark of nonequilibrium physics, quantifying irreversibility, dissipation, and the efficiency of energy transduction processes. Despite many efforts, its measurement at the nanoscale remains challenging. We introduce a variance sum rule (VSR) for displacement and force variances that permits us to measure the entropy production rate σ in nonequilibrium steady states. We first illustrate it for directly measurable forces, such as an active Brownian particle in an optical trap. We then apply the VSR to flickering experiments in human red blood cells. We find that σ is spatially heterogeneous with a finite correlation length, and its average value agrees with calorimetry measurements. The VSR paves the way to derive σ using force spectroscopy and time-resolved imaging in living and active matter.

Nonequilibrium steady states (NESS) pervade nature, from climate dynamics (*1*) to living cells and active matter (*2*). A fundamental quantity is the entropy production rate σ at which energy is dissipated to the environment, which is positive by the second law of thermodynamics (*3*, *4*). Entropy production measurements remain challenging despite their relevance, especially in microscopic systems with stochastic and spatially varying fluctuations and limited access to microscopic variables (*5*, *6*). The entropy production rate σ determines the efficiency of energy transduction in classical and quantum systems (*7*, *8*), the energetic costs and irreversible behavior of living cells (*9*–*12*). It is an elusive quantity when forces and currents are experimentally inaccessible. Bounds can be obtained from time irreversibility (*13*, *14*), the thermodynamic uncertainty relation (*15*, *16*), and coarse-graining (*17*–*21*). Most of these results provide lower bounds that refine the second law of thermodynamics, $\sigma \geq 0$. However, the bounds are often loose without upper limits and therefore uninformative about the actual σ. Alternative methods that estimate σ more precisely are needed to determine dissipative processes in the nanoscale.

Variance sum rule

We introduce a variance sum rule (VSR) to derive σ in experiments where a measurement probe is in contact with a system in a NESS (Fig. 1A). Dynamics are described by a Langevin equation, $\dot{x}(t) = \mu F_t + \sqrt{2D}\eta_t$, with probe mobility μ, diffusivity D, and a Gaussian white noise term, η_t. The total force acting on the probe $F_t \equiv F_t(x_t)$ equals the sum of the force exerted by the measurement device, F_t^{M}, plus a probe-system interaction, F_t^{I}, $F_t = F_t^{\mathrm{M}} + F_t^{\mathrm{I}}$ (arrows in Fig. 1A). In most experimental settings, F_t^{I} remains inaccessible, so F_t and σ cannot be directly measured. Our approach focuses on how observables Q_t on average spread in time, as quantified by their variance $\mathcal{V}_Q(t) = \overline{Q_t^2} - \overline{Q_t}^2$ with $\overline{(\ldots)}$ the dynamical average in the NESS. The VSR is an equality for integrated quantities in an arbitrary time interval $(0, t)$, which imposes a tight constraint on the fluctuations in a stochastic diffusive system over the experimental timescales. By integrating the Langevin equation over the interval $(0,t)$ and by taking the variance of both sides, a time-preserved identity can be obtained (materials and methods S1). The VSR for position and force fluctuations reads

$$\mathcal{V}_{\Delta x}(t) + \mu^2 \mathcal{V}_{\Sigma_{\mathrm{F}}}(t) = 2Dt + S(t) \qquad (1)$$

where the left-hand side includes the variances of the displacements $\Delta x_t = x_t - x_0$, and of time-cumulative forces $[\Sigma_F(t) = \int_0^t ds F_s]$. The total variance $\mathcal{V}_{\mathrm{T}}(t) = \mathcal{V}_{\Delta x}(t) + \mu^2 \mathcal{V}_{\Sigma_F}(t)$ equals the free diffusion term $2Dt$ plus a nonequilibrium contribution $S(t)$ denoted as excess variance

$$S(t) = 2\mu \int_0^t ds [C_{xF}(s) - C_{Fx}(s)] \qquad (2)$$

that measures the breakdown of time-reversal symmetry, with $C_{AB}(s) = \overline{A_s B_0} - \overline{A}_s \, \overline{B}_0$ the correlation function in the NESS. In equilibrium, $S(t) = 0$ because of time-reversal s metry. Figure 1B illustrates the VSR f generic NESS.

From the VSR, one can derive an equation relating σ to the variances of fluctuating variables. By taking the time derivative twice of Eq. 2 and evaluating it at $t = 0$, one obtains a formula for σ that depends on the convexity of the excess variance $S(t)$ at $t = 0$ (materials and methods S2),

$$\sigma = \frac{v^2}{\mu} + \frac{1}{4\mu} \partial_t^2 S|_{t=0} \qquad (3)$$

where $v = \overline{\dot{x}}$ is the particle's average velocity and σ is expressed in power units (e.g., $k_{\mathrm{B}}T/\mathrm{s}$). By using Eq. 1 along with Eq. 3, we derive the formula for the rate of entropy production in terms of the static variance of the force $\mathcal{V}_{\mathrm{F}} = \overline{F^2} - \overline{F}^2$ and the convexity of the mean-squared displacement $\mathcal{V}_{\Delta x}$ at time 0

$$\sigma = \frac{v^2}{\mu} + \frac{1}{4\mu} \partial_t^2 \mathcal{V}_{\Delta x}|_{t=0} + \frac{\mu}{2} \mathcal{V}_{\mathrm{F}} \qquad (4)$$

To illustrate the VSR, we consider two examples of a NESS where F_t equals the force in the measurement device, $F_t = F_t^{\mathrm{M}}$, and $F_t^{\mathrm{I}} = 0$.

Methods

Experiments with colloidal particles (Figs. 1 and 2) were done in a miniaturized version of an optical tweezers instrument described in (*22*). Human red blood cells (RBCs) were obtained by finger pricking of a healthy donor for the RBC experiments. The phosphate-buffered saline (PBS) solution contains 130 mM NaCl, 20 mM K/Na phosphate buffer, 10 mM glucose, and 1 mg/ bovine serum albumin per milliliter of solution. For optical tweezer (OT)-stretching experiments, 4 μl of blood was diluted in 1 ml of PBS. RBCs were treated and biotinylated for OT sensing as described in (*11*). For optical microscopy (OM) measurements, the RBC pellet obtained after centrifugation (5000*g* for 10 min at 4°C) was resuspended (1:15) in PBS solution (*23*). Contact areas in OT experiments were estimated using a multiscale feature extractor based on a Gaussian pyramid representation of the raw image followed by a Laplacian reconstruction. For OT sensing, we used estimates from (*11*).

Bead dragged through water

The first system is an optically trapped colloidal particle dragged through water (friction coefficient $\gamma = 1/\mu$) at speed v. The bead's dynamics can be analytically solved, and the VSR (Eq. 1) verified (materials and methods S3). Equation 4 follows with $S = 0$ and $\sigma = \gamma v^2$, as expected. Figure 1C shows the experimental validation of the VSR (Eq. 1). The right inset shows measurements of $\sigma - \gamma v^2$ for several repetitions of the experiment and

---

[1]Max Planck Institute for the Physics of Complex Systems, Nöthnitzer Straße 38, 01187 Dresden, Germany. [2]Dipartimento di Fisica e Astronomia, Università di Padova, Via Marzolo 8, 35131 Padova, Italy. [3]Small Biosystems Lab, Condensed Matter Physics Department, Universitat de Barcelona, C/ Marti i Franques 1, 08028 Barcelona, Spain. [4]Department of Medical Biochemistry and Cell Biology, Institute of Biomedicine, The Sahlgrenska Academy, University of Gothenburg, 40530 Gothenburg, Sweden. [5]Facultad de Ciencias Experimentales, Universidad Francisco de Vitoria, Ctra. Pozuelo-Majadahonda Km 1,800, 28223 Pozuelo de Alarcón, Madrid, Spain. [6]Third Institute of Physics, Georg August Universität Göttingen, Göttingen, Germany. [7]Cluster of Excellence "Multiscale Bioimaging: from Molecular Machines to Networks of Excitable Cells" (MBExC), University of Göttingen, Göttingen, Germany. [8]Departamento de Química Física, Facultad de Química, Universidad Complutense, 28040 Madrid, Spain. [9]Translational Biophysics, Instituto de Investigación Sanitaria Hospital Doce de Octubre (IMAS12), Av. Andalucía, 28041 Madrid, Spain. [10]INFN, Sezione di Padova, Via Marzolo 8, 35131 Padova, Italy. [11]Institut de Nanociència i Nanotecnologia (IN2UB), Universitat de Barcelona, 08028 Barcelona, Spain.
***Corresponding author. Email: ritort@ub.edu**
†These authors contributed equally to this work.

using Eq. 4, finding $\sigma - \gamma v^2 = -5 \pm 7\ k_{\mathrm{B}}T/\mathrm{s}$. Notice that $S = 0$ implies that the two rightmost terms in Eq. 4 are of equal magnitude but opposite sign, compensating each other, $\mu\mathcal{V}_F = -\frac{1}{2\mu}\partial_t^2\mathcal{V}_{\Delta x}|_{t=0} = k_{\mathrm{B}}T/\tau_r > 0$ with $\tau_r = \gamma/k = 0.35$ ms the bead's relaxation time ($k = 70$ pN/μm being the trap stiffness). The value $\mu\mathcal{V}_{\mathrm{F}} \sim 3 \times 10^3\ k_{\mathrm{B}}T/\mathrm{s}$ is almost three orders of magnitude larger than $\sigma - \gamma v^2$ ($\pm 7\ k_{\mathrm{B}}T/\mathrm{s}$).

The results $S = 0$ and $\sigma = \gamma v^2$ are not restricted to a harmonic well but hold for an arbitrary time-dependent potential $U(x - vt)$. This gives a reversed thermodynamic uncertainty relation (*16*) for the work exerted on the bead by the optical trap, $W_t = v\Sigma_F(t) = v\int_0^t ds F_s$, and an upper bound for σ (materials and methods S4),

$$\frac{\sigma}{k_{\mathrm{B}}T} \le \frac{2\overline{W_t}^2}{t\,\mathcal{V}_W(t)} \tag{5}$$

In Fig. 1C (left inset), we experimentally test Eq. 5. The upper bound becomes tight for $t \gg \tau_r$, the difference between two terms in Eq. 5 vanishing as τ_r/t, as expected from the steady-state fluctuation theorem for Gaussian work distributions (*4*).

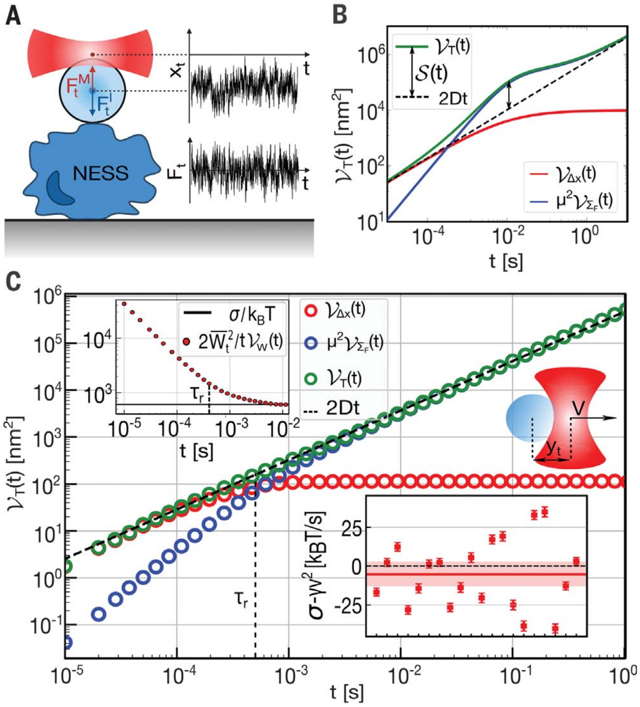

Fig. 1. Variance sum rule (VSR): Sketches and experiments with a dragged particle. (**A**) Experimental setup for a NESS measured with optical tweezers. (**B**) Illustration of the VSR showing the different terms in Eq. 1. (**C**) Experimental test of the VSR for an optically trapped bead dragged through water at room temperature (bead radius $R = 1.5$ μm, mobility $\mu = 4 \times 10^4$ nm/pN · s, speed $v = 10$ μm/s, $\gamma v^2 = 610\ k_{\mathrm{B}}T/s$). The lower inset plots $\sigma - \gamma v^2 = \frac{1}{4\mu}\partial_t^2\mathcal{V}_{\Delta x}|_{t=0} + \frac{\mu}{2}\mathcal{V}_F$ from Eq. 4 for the experimental realizations; the horizontal red line shows the average over all experiments [$-5 \pm 7\ k_{\mathrm{B}}T/s$] with one standard deviation (red band). The black dashed line is the theoretical prediction $\sigma = \gamma v^2$. The upper inset shows the experimental test of the inequality (Eq. 5). Dashed vertical lines show the bead's relaxation time τ_r.

The stochastic switching trap

The second system we consider is the stochastic switching trap (SST) (*22*), where an active force is applied to an optically trapped bead by randomly switching the trap position λ_t between two values (λ_+, λ_-) separated by $\Delta\lambda = \lambda_+ - \lambda_-$ (Fig. 2A). Jumps occur at exponentially distributed times with switching rates w_+, w_- at each position. The ratio $w_-/w_+ = q/(1-q)$ defines the probability q of the trap to be at position λ_+. Figure 2B shows the measured bead's position x_t and force $F_t = k(\lambda_t - x_t)$ for three cases with $q = 1/2$ and varying $\Delta\lambda$. The bead follows the movement of the trap (top), quickly relaxing to its new equilibrium trap position at every jump (force spikes, bottom). Figure 2C shows the total variance, $\mathcal{V}_{\mathrm{T}}(t) = \mathcal{V}_{\Delta x}(t) + \mu^2\mathcal{V}_{\Sigma_F}(t)$. $\mathcal{V}_T$ deviates from $2Dt$ (dashed line) between 10^{-4} and 1 s, showing that $S \neq 0$ is comparable to $\mathcal{V}_{\mathrm{T}}$ (notice the log-log scale). The SST model is analytically solvable (materials and methods S5), giving expressions for $\mathcal{V}_{\Delta x}(t), \mathcal{V}_{\Sigma_F}(t)$, and $S(t)$. For the latter, we find

$$S(t) = 4(\Delta\lambda)^2 q(1-q) \times \frac{\alpha(1-e^{-w_r t}) - \alpha^2(1-e^{-wt})}{1-\alpha^2} \tag{6}$$

with $w = w_+ + w_-$, $\alpha = w_r/w$, and $w_r = 1/\tau_r = k/\gamma$ (the bead's relaxation rate for a resting trap). In Fig. 2C, we test the VSR and Eq. 6 for three NESS conditions. The inset shows the two terms contributing to the total variance $\mathcal{V}_{\mathrm{T}}$. For large times, S converges to a finite value, and $\mathcal{V}_{\mathrm{T}}$ merges with the equilibrium line $2Dt$ (black dashed line) when plotted in log-log scale. Equations 3 and 6 yield the theoretical prediction ($v = 0$)

$$\sigma_{\mathrm{th}} = (k\Delta\lambda)^2 q(1-q)\mu\frac{w}{w+w_r} \tag{7}$$

Figure 2D shows values of σ measured in SST experiments with $\Delta\lambda = 280$ nm using Eq. 4. Their average $\sigma_{\mathrm{exp}} = 4.6 \pm 4 \times 10^3\ k_{\mathrm{B}}T/\mathrm{s}$ agrees with the theoretical prediction (Eq. 7), $\sigma_{\mathrm{th}} \sim 5.3 \times 10^3\ k_{\mathrm{B}}T/\mathrm{s}$. Figure 2E compares σ_{exp} with σ_{th} (Eq. 7) (black dashed line) for varying $\Delta\lambda$. Experiment and theory agree over three decades of σ.

Reduced VSR

Until now, we have considered the case of a single degree of freedom where the total force acting on the bead equals the measured force, $F_t = F_t^{\mathrm{M}}$ and $F_t^{\mathrm{I}} = 0$. For the case of multiple degrees of freedom where positions and total forces can be measured, Eqs. 1 and 3, can be generalized (materials and methods S1 and S2). Quite often, however, a measurement probe (atomic force microscope tip, microbead, etc.) is in contact with a system in a NESS, such as a biological cell with metabolic activity (Fig. 1A). In this case, $F_t^{\mathrm{I}} \neq 0$ is experimentally inaccessible, and $F_t = F_t^{\mathrm{M}} + F_t^{\mathrm{I}}$ cannot be measured, making the VSR (Eq. 1) inapplicable. Moreover, in many cases, only a spatial degree of freedom x_t is monitored, e.g., in particle-tracking experiments (*24*, *25*) or in detecting cellular fluctuations (*26*, *27*). To apply the VSR in these situations, it is necessary to model the NESS by making assumptions about the interaction F_t^{I} and the underlying degrees of freedom. Specifically, for a linear-response measuring device ($F_t^{\mathrm{M}} = -kx_t$), a reduced VSR for a single degree of freedom can be derived and expressed in terms of variances related to the position x_t only. In these conditions, the displacement variance, $\mathcal{V}_{\Delta x}$, along with the variance of $\Sigma_x(t) = \int_0^t ds\ x_s$, $\mathcal{V}_{\Sigma_x}(t)$, satisfy (materials and methods S6),

$$\mathcal{V}_{\Delta x}(t) + \mu^2 k^2\ \mathcal{V}_{\Sigma_x}(t) = 2Dt + \tilde{S}(t) \tag{8}$$

Equation 8 is a general result which, however, does not permit one to derive a formula for σ like Eq. 3. Notice that $\tilde{S}$ differs from S in Eq. 1 and does not vanish in equilibrium. $\tilde{S}$ can be expressed in terms of the generic interacting force F_t^{I}; see eq. S38 in materials and methods. To derive σ using Eq. 8, we use a solvable model for the experiment and a procedure consisting of the following steps: (i) Analytically derive expressions for the excess variances, $S(t)$ and $\tilde{S}(t)$ for the model; (ii) calculate σ_{th} from $S(t)$ using Eq. 3; (iii) fit the reduced VSR (Eq. 8) to the experimental data using $\tilde{S}(t)$ from the model to extract the model parameters; (iv) insert the parameters in the analytical expression for σ_{th}

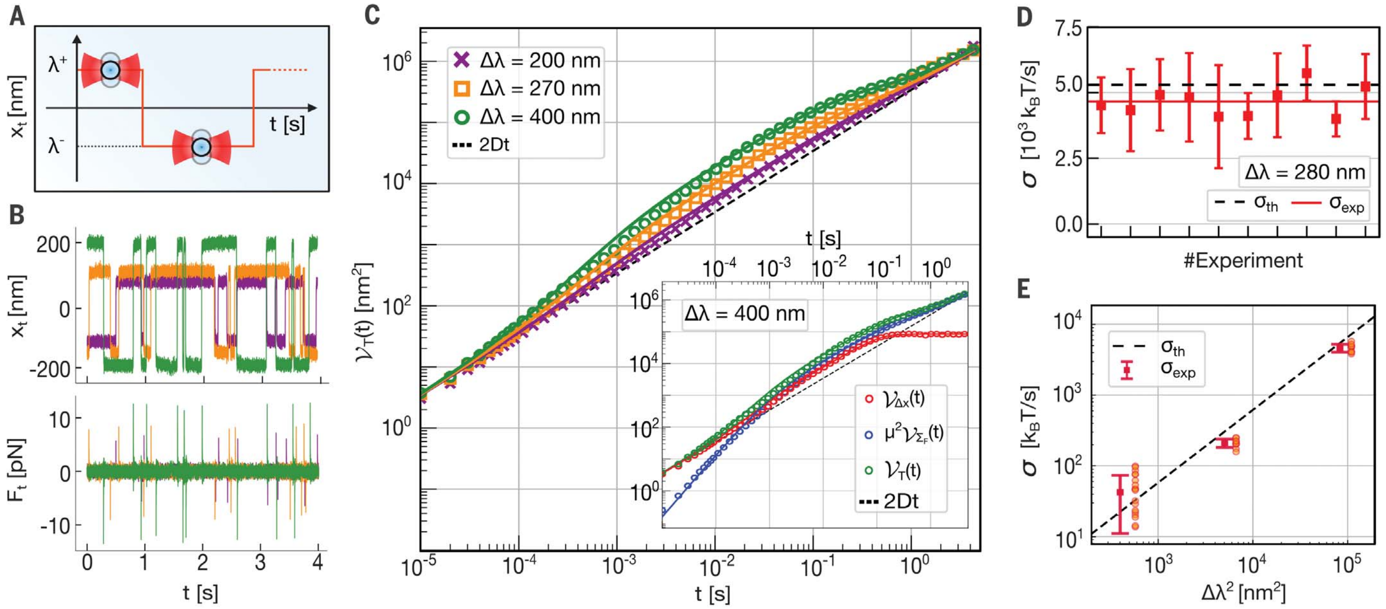

Fig. 2. VSR and entropy production rate for experiments with a stochastic switching trap. (**A**) Schematics of the experiment. (**B**) Traces of position and force for three $\Delta\lambda$ values [see legend in (C)]. (**C**) VSR (Eq. 1) and total variance $\mathcal{V}_T$: Symbols are experimental data, and lines represent the theory with known parameters without fitting. The inset shows the different terms in the VSR. (**D**) Measurements of σ for $w_+ = w_- = 10$ s^{-1} and $\Delta\lambda = 280$ nm; we show different experimental realizations (squares), their average σ_{exp} and the theoretical value σ_{th} (Eq. 7). (**E**) σ (red symbols) averaged over experimental realizations (orange circles) for $\Delta\lambda$ = 18, 70, and 280 nm; black line is the analytical prediction (Eq. 7).

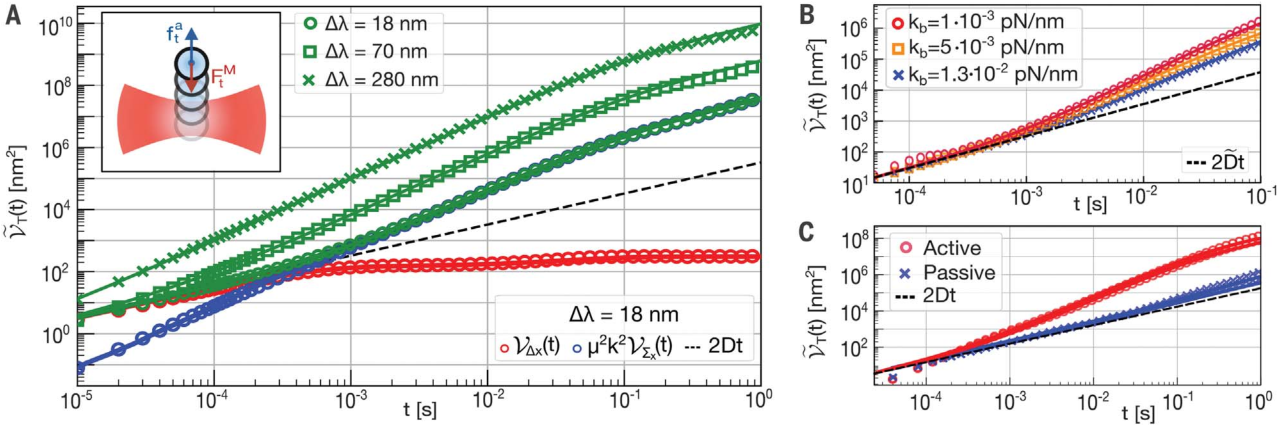

Fig. 3. Application of the reduced VSR to experiments (SST and RBCs) to extract the entropy production rate. (**A**) Test of Eq. 8 for the SST experimental data, equivalent to the active ABP, in a harmonic trap (Eq. 9 and inset). Symbols are experimental values for $\tilde{\mathcal{V}}_T(t) = \mathcal{V}_{\Delta x}(t) + \mu^2k^2\ \mathcal{V}_{\Sigma_x}(t)$, fitted to Eq. 8 for different $\Delta\lambda$ (lines). Blue and red circles are the two contributions to $\tilde{\mathcal{V}}_T(t)$ for $\Delta\lambda = 18$ nm. (**B** and **C**) Fits of the reduced VSR to $\tilde{\mathcal{V}}_T(t)$ for the two-layer active model (materials and methods S6). (B) Healthy RBCs in OT-stretching experiments at three trap stiffness values (Fig. 4A). To help visualization, the three different $\tilde{\mathcal{V}}_T(t)$ values have been scaled with respect to a single $\tilde{D}$ value; (C) Healthy (active) and passive RBCs in OT-sensing experiments (Fig. 4B).

to derive σ. The approach remains applicable to a vast category of NESS whenever the interacting force F_{I} between the probe and NESS is linear. This is a typical situation in mesoscopic systems where fluctuations are small in the linear response regime. A model for the experimental system that includes the degrees of freedom contributing most to σ is required.

For instance, consider an active Brownian particle (ABP) in an optical trap subject to a random time-correlated active force $F_t^{\text{I}} \equiv f_t^{\text{a}}$ of amplitude ϵ, $\overline{f_t^{\text{a}}} = 0$, $\overline{f_t^{\text{a}}f_s^{\text{a}}} = \epsilon^2 e^{-|t-s|/\tau_{\text{a}}}$, with τ_{a} the active correlation time (Fig. 3A, inset). The dynamics are described by the stochastic equation

$$\dot{x}_t = -k\mu x_t + \sqrt{2D}\eta_t + \mu f_t^{\text{a}} \qquad (9)$$

with k the trap stiffness, μ the particle mobility, and $D = k_{\text{B}}T\mu$ the diffusion constant. To test the reduced-VSR approach (Eq. 8) for deriving σ, we exploit the mapping of the ABP (Eq. 9) to the SST model discussed previously (Fig. 2A). The mapping follows by identifying parameters $\epsilon = k\Delta\lambda\sqrt{q(1-q)}$, $\tau_{\text{a}} = 1/w$, $w_r = k\mu$ from which Eq. 7 follows [for $q = 1/2$, see also (*28*)]. We have used Eq. 8 to analyze the data already used in the previous approach for the SST experiments (Fig. 2) with $\tilde{S}(t) = 2\epsilon^2\mu^2\tau_a\left[t - \tau_{\text{a}}\left(1 - e^{-t/\tau_{\text{a}}}\right)\right]$(compare eq. S37) where ϵ and τ_{a} are fitting parameters. Results are shown in Fig. 3A and residuals in fig. S2A. Their values and σ agree with the

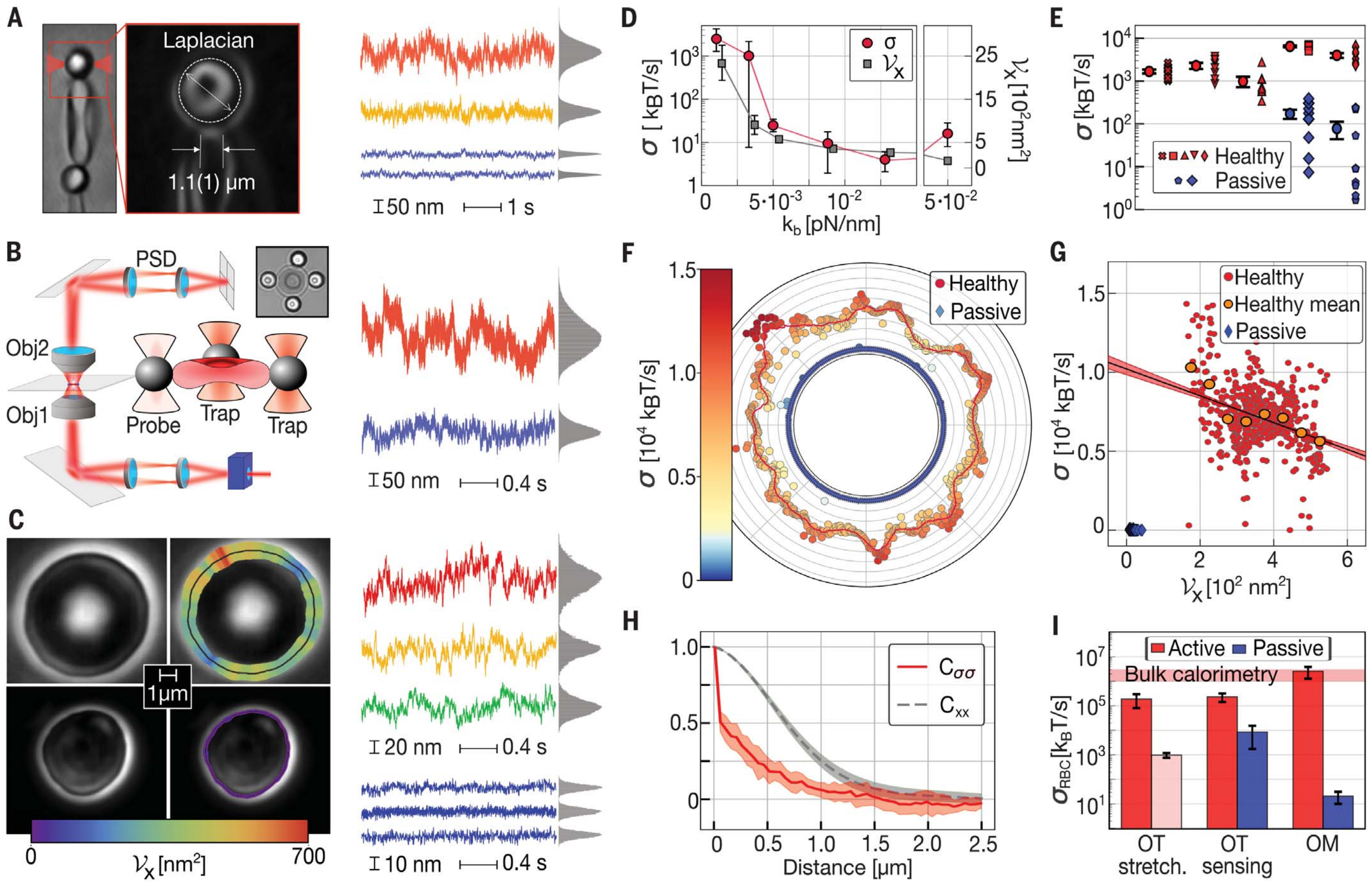

Fig. 4. Application of the reduced VSR to RBCs. (**A**) OT-stretching experiments. Video image of stretched RBC and schematics of contact area estimation (left); (right) three selected bead position traces at a high (blue), medium (orange), and low (red) trap stiffness. (**B**) OT-sensing experiments. Experimental setup from (*11*) (left) and tracking bead position traces for a healthy (red) and passive (blue) RBC (right). (**C**) Ultrafast OM measurements: Healthy RBC (upper images) and position traces (right) for three selected pixels (50 nm by 50 nm) along the cell contour with high (red), medium (yellow), and low (green) variance $\mathcal{V}_x$; passive RBC (lower images) and cell contour traces for three selected pixels (blue, right). The right images also show a color variance map along the cell contour. The color bar denotes variance levels (red, highest; blue, lowest). (**D**) σ and position variance V_x measurements for OT stretching (A) varying the trap stiffness k_b from high values (5×10^{-2} pN/nm, rightmost points) to low values (7×10^{-4} pN/nm, leftmost points) for healthy RBCs. (**E**) σ measurements for OT sensing for healthy (red symbols) and passive (blue symbols) RBCs. (**F**) Colored σ map for OM measurements along the equatorial cell contour, as in (C), for a healthy RBC (circles) and a passive RBC (diamonds). The radial distance represents σ in arbitrary units. The orange curve is the σ-smoothed profile. (**G**) Scatter plot of σ versus $\mathcal{V}_x$ for the RBCs of (F), showing that they are partially anticorrelated. Orange circles are σ values averaged over windows of 50 nm^2 in $\mathcal{V}_x$. (**H**) Spatial correlation functions for σ and position *x* are measured along the cell contour. (**I**) Values of σ_{RBC} compared to calorimetry estimates. For OT stretching, the dark (light) red bar corresponds to the lowest (highest) trap stiffness.

expected ones (table S1 and fig. S3A.). Therefore, the reduced VSR (Eq. 8) permits us to infer NESS parameters and σ from x_t measurements only.

Red blood cells

Finally, we apply the reduced-VSR to the challenging case of human RBCs (*29*). RBCs metabolize glucose into adenosine 5´-triphosphate (ATP) via the glycolytic pathway, producing the cell membrane's active flickering with a consequent entropy creation (*11, 23, 30, 31*). The RBC membrane is dynamically attached to the spectrin cortex through multiprotein complexes, which actively bind and unbind in the phosphorylation step of the glycolytic pathway (*32*). We have carried out experimental RBC measurements using three techniques (Fig. 4). Two of them use OTs in different setups: (i) mechanical stretching of RBCs using beads nonspecifically attached to the membrane with different optical trap stiffness (OT stretching, Fig. 4A); (ii) mechanical sensing of a biotinylated RBC membrane using streptavidin functionalized beads using data from (*11*) (OT sensing, Fig. 4B). The third technique measures cell contour fluctuations by membrane flickering segmentation tracking of free-standing RBCs using ultrafast OM (*23, 33*) (Fig. 4C). As a first observation, a single-layer active model (Eq. 9) with its $\tilde{S}(t)$ in Eq. 8 does not describe the experimental data. Instead, we consider a two-layer model with one hidden position variable for the active membrane–cortex interaction that is linearly coupled to the membrane outer layer x (probe) (materials and methods S7). Similar active models have been proposed in the study of hair-cell bundle dynamics (*14, 34, 35*). The two-layer active model leads to a reduced VSR of the form (Eq. 8) that fits the experimental data; the fitting procedure is described in materials and methods S8 and S9. Some fits of the reduced VSR are shown in Fig. 3, B and C, and residuals of the fits are shown in fig. S2, B to F.

Figure 4, D and E, show σ values obtained from OT-stretching data in the range of trap stiffnesses $k_b = 5 \times 10^{-2} - 7 \times 10^{-4}$ pN/nm and OT-sensing data with $k_b \sim 2 \times 10^{-5}$ pN/nm for healthy and ATP-depleted (passivated) RBCs. For OT stretching, σ increases as k_b decreases reaching $\sigma = (3 \pm 1) \times 10^3\ k_\mathrm{B}T/\mathrm{s}$ averaged over RBCs, for the lowest k_b. This value is compatible with OT-sensing measurements, $\sigma = (2 \pm 1) \times 10^3\ k_\mathrm{B}T/\mathrm{s}$ for healthy RBCs, which is larger than for passive RBCs (red and blue symbols in Fig. 4E). Moreover, σ appears correlated with the variance of the flickering signal as measured from the position traces, $\mathcal{V}_x = \overline{x^2} - \overline{x}^2$ (Fig. 4D). The apparent correlation demonstrates that the probe stiffness k_b must be lower than the stiffness of the RBC, $k_\mathrm{RBC} \sim 5 \times 10^{-3}$ pN/nm, to measure σ; otherwise, the active flickering of the RBC membrane is suppressed by the passive fluctuations of the bead. The correlation between σ and V_x is also explicitly shown in fig. S4, where a color-map plot of the stiffness shows that we can detect active flickering and σ only for $k_b < k_\mathrm{RBC}$. Indeed, for the largest trap stiffness $k_b \sim 5 \times 10^{-2}$ pN/nm, one obtains $\sigma \sim 10\ k_\mathrm{B}T/\mathrm{s}$ (rightmost points in Fig. 4D), a value almost constant if the RBC is stretched up to 30 pN (fig. S4). The measured σ is extensive with the bead–RBC contact area. Estimations from video images (Fig. 4A and materials and methods) yield circular contact areas of $a = 0.8 \pm 0.2\,\mu\mathrm{m}^2$ for both OT-type experiments giving the heat flux density $j_\sigma = \sigma/a = (3 \pm 1) \times 10^3\ k_\mathrm{B}T/(\mathrm{s} \cdot \mu\mathrm{m}^2)$ for OT stretching at low k_OT and $j_\sigma = (1.8 \pm 0.6) \times 10^3\ k_\mathrm{B}T/(\mathrm{s} \cdot \mu\mathrm{m}^2)$ for OT sensing. Such estimations are subject to uncertainty in the actual diameter and shape of the contact area. Furthermore, we have analyzed the simulation data of the OT-sensing experiments based on the three-dimensional numerical model of (*11*). The active and passive trajectories for the sensing bead give $\sigma \sim 10^4\ k_\mathrm{B}T/\mathrm{s}$ and $\sigma \sim 20\ k_\mathrm{B}T/\mathrm{s}$, respectively (materials and methods S10).

For the OM experiments, we show in Fig. 4C the color map of the position variance $\mathcal{V}_x$ (healthy, top; passive, bottom), and in Fig. 4F we show the color map of σ (circles, healthy; diamonds, passive), measured over pixels of area 50 nm by 50 nm along the RBC contour. For the healthy RBCs, both σ and $\mathcal{V}_x$ reveal an RBC heterogeneous activity with average values $\sigma = (7 \pm 1) \times 10^3\ k_\mathrm{B}T/\mathrm{s}$ and $\mathcal{V}_x = 400 \pm 10\ \mathrm{nm}^2$. Molecular maps of heterogeneous RBC deformability have been previously reported (*36*). In contrast to OT experiments (Fig. 4, D and E), for OM experiments σ and $\mathcal{V}_x$ are anticorrelated in the active regime (Pearson coefficient ~ -0.4) with high-variance regions showing lower σ (Fig. 4G). Results for other RBCs are shown in fig. S5. This counterintuitive result demonstrates the critical role of the active timescale τ_a, which, for fixed ϵ, determines the active contribution to the total variance, $\mathcal{V}_x = \mathcal{V}_x^\mathrm{passive} + \alpha(\tau_\mathrm{a})\sigma(\tau_\mathrm{a})$ (eq. S41a) with $\alpha(\tau_\mathrm{a})$ positive and monotonically increasing with τ_a and $\sigma(\tau_\mathrm{a})$ given in eq. S42. It can be shown that in the high-activity limit $\tau_\mathrm{a} \to 0$, $\sigma(\tau_\mathrm{a})$ saturates to a finite value whereas $\alpha(\tau_\mathrm{a}) \sim \tau_\mathrm{a}$, decreasing $\mathcal{V}_x$ (fig. S6). We hypothesize that the anticorrelation observed in the σ map derives from the highly heterogeneous τ_a (mean 0.05 s and standard deviation 0.2 s) but nearly constant ϵ (mean 4.4 pN and standard deviation 0.2 pN) across all pixel units. A constant-noise amplitude ϵ with a heterogeneous τ_a suggests a uniform density of kickers but a heterogeneous ATP concentration c_ATP across the RBC surface, which modulates the ATP binding rate of the kickers, $\tau_\mathrm{a}^{-1} \sim k_\mathrm{bind} \propto c_\mathrm{ATP}$.

The σ map of a single RBC determines the finite correlation length ξ for the spatially varying σ field, a main prediction of active field theories (*37*, *38*) and stochastic hydrodynamics (*39*). For healthy RBCs, ξ has been estimated from the spatial correlation function $C_{\sigma\sigma}(d)$, and $C_{xx}(d)$ of the traces at a curvilinear distance d along the RBC contour, Fig. 4H. Functions can be fitted to an exponential $\sim\exp(-d/\xi)$ with $\xi_{\sigma\sigma} \sim 0.35 \pm 0.05\,\mu\mathrm{m}$ and $\xi_{xx} \sim 0.82 \pm 0.02\ \mu\mathrm{m}$, giving the median $\xi \sim 0.6 \pm 0.2\,\mu\mathrm{m}$. This value is larger than the lateral resolution of the microscope (200 nm). The structure factor of the σ field along the cell contour shows a characteristic peak at a domain length $l \sim 1.3\ \mu\mathrm{m}$, which is larger than $\xi_{\sigma\sigma}$, possibly due to the heterogeneous cortex-membrane binding-unbinding dynamics that produce differently active σ domains (materials and methods S11). A two-layer active model in a ladder with an interlayer coupling k_{xx} further corroborates the value obtained for ξ_{xx} (materials and methods S12). The average heat flux density can be estimated as $j_\sigma = \sigma/\xi^2 = (2 \pm 1) \times 10^4\ k_\mathrm{B}T/(\mathrm{s} \cdot \mu m^2)$ with ξ^2 the typical area of an entropy-producing region. In summary, for an RBC of typical surface area $A \sim 130\ \mu\mathrm{m}^2$, one obtains $\sigma_\mathrm{RBC} = j_\sigma \times A = (2 \pm 1) \times 10^5\ k_\mathrm{B}T/\mathrm{s}$ (OT stretching, at lowest k_b); $\sigma_\mathrm{RBC} = (2 \pm 1) \times 10^5\ k_\mathrm{B}T/\mathrm{s}$ (OT sensing); and $\sigma_\mathrm{RBC} = (3 \pm 1) \times 10^6\ k_\mathrm{B}T/\mathrm{s}$ (OM). These values are compatible with calorimetric bulk measurements of packed RBCs, $\sigma_\mathrm{RBC}^\mathrm{bulk} = (2 \pm 1) \times 10^6 k_\mathrm{B}T/\mathrm{s}$ (*40*, *41*) and are larger than indirect measures based on the breakdown of the fluctuation-dissipation theorem and effective temperatures (*11*, *42*). The significantly low σ values obtained for passive RBCs (blue data in Fig. 4, E to G and I) validate our approach. Our $\sigma_\mathrm{RBC} \sim 10^5$–$10^6\ k_\mathrm{B}T/\mathrm{s}$ is higher than the values obtained through information-theoretic measures based on the breakdown of detailed balance (*12*, *14*). Intuitively, the VSR (Eqs. 1 and 8) sets an energy balance between fluctuating positions and forces, both conjugated energy variables, a missing feature in the thermodynamic uncertainty relation and coarse-graining models (*43*–*45*). In general, the VSR captures most of σ because sampling rates, 40 kHz for OT stretching, 25 kHz for OT sensing, and 2 kHz for OM, are higher than the frequency of the active noise, ~100 s^{-1} for the RBC experiments (tables S2 to S4).

Discussion

The agreement between mechanical and bulk calorimetric estimates of the RBC metabolic energy turnover suggests that the heat produced in the glycolytic pathway is tightly coupled with membrane flickering due to active kickers. Tight mechanochemical coupling is critical to an efficient free-energy chemical transduction. It has been observed in processive enzymes (e.g., polymerases, transport motors, etc.) (*46*) and in allosteric coupling in ligand binding (*47*). Tightly coupled processes are related to emergent cycles in cellular metabolism and chemical reaction networks, particularly for the relevant glycolytic cycle of RBCs (*48*). A clarifying example of weak versus tight coupling is the effect of the trap stiffness in deriving σ (Fig. 4D). Unless the probe stiffness is smaller than the RBC stiffness, the probe's passive fluctuations mask the system's activity and σ. In addition to molecular motors and living cells, the VSR should apply to time-resolved photoacoustic calorimetry (*49*) and enzyme catalysis, where the effective diffusion constant of the enzyme increases linearly with the heat released (*50*), a consequence of Eq. 1. Moreover, spatially resolved maps of partial measurements of σ for weak mechanochemical coupling provide insight into the structural features underlying heat dissipation in biological cells. In a wider context, the VSR applies to nonlinear systems, from non-Gaussian active noise to nonlinear potentials (materials and methods S13). Finally, we stress that different models can fit the experimental data. However, the power of the VSRs, Eqs. 1 and 8, is given by the constraint imposed by the sum of variances over the experimental timescales. By fitting the experimental data to a single function, the total variance $\mathcal{V}_\mathrm{T}(t)$ over several decades, the contribution of dissipative processes over multiple timescales is appropriately weighted in the sum balance. This distinguishes our approach from plain model fitting of the experimental power spectrum to derive the model parameters (*35*) that may lead to inaccurate estimations (materials and methods S14). In this regard, the VSR links modeling with energetics.

REFERENCES AND NOTES

1. M. S. Singh, M. E. O'Neill, *Rev. Mod. Phys.* **94**, 015001 (2022).
2. C. Bechinger *et al.*, *Rev. Mod. Phys.* **88**, 045006 (2016).
3. C. Maes, *Séminaire Poincaré* **2**, 29 (2003).
4. U. Seifert, *Rep. Prog. Phys.* **75**, 126001 (2012).
5. F. Ritort, *Adv. Chem. Phys.* **137**, 31–123 (2008).
6. S. Ciliberto, *Phys. Rev. X* **7**, 021051 (2017).
7. I. A. Martínez *et al.*, *Nat. Phys.* **12**, 67–70 (2016).
8. G. T. Landi, M. Paternostro, *Rev. Mod. Phys.* **93**, 035008 (2021).
9. P. Martin, A. J. Hudspeth, F. Jülicher, *Proc. Natl. Acad. Sci. U.S.A.* **98**, 14380–14385 (2001).
10. C. Battle *et al.*, *Science* **352**, 604–607 (2016).
11. H. Turlier *et al.*, *Nat. Phys.* **12**, 513–519 (2016).

12. C. W. Lynn, E. J. Cornblath, L. Papadopoulos, M. A. Bertolero, D. S. Bassett, *Proc. Natl. Acad. Sci. U.S.A.* **118**, e2109889118 (2021).
13. J. Li, J. M. Horowitz, T. R. Gingrich, N. Fakhri, *Nat. Commun.* **10**, 1666 (2019).
14. É. Roldán, J. Barral, P. Martin, J. M. Parrondo, F. Jülicher, *New J. Phys.* **23**, 083013 (2021).
15. A. C. Barato, U. Seifert, *Phys. Rev. Lett.* **114**, 158101 (2015).
16. J. M. Horowitz, T. R. Gingrich, *Nat. Phys.* **16**, 15–20 (2020).
17. G. Bisker, M. Polettini, T. R. Gingrich, J. M. Horowitz, *J. Stat. Mech.* **2017**, 093210 (2017).
18. G. Teza, A. L. Stella, *Phys. Rev. Lett.* **125**, 110601 (2020).
19. D. J. Skinner, J. Dunkel, *Proc. Natl. Acad. Sci. U.S.A.* **118**, e2024300118 (2021).
20. A. Dechant, S.-i. Sasa, *Phys. Rev. X* **11**, 041061 (2021).
21. C. Dieball, A. Godec, *Phys. Rev. Lett.* **129**, 140601 (2022).
22. E. Dieterich, J. Camunas-Soler, M. Ribezzi-Crivellari, U. Seifert, F. Ritort, *Nat. Phys.* **11**, 971–977 (2015).
23. R. Rodríguez-García *et al*., *Biophys. J.* **108**, 2794–2806 (2015).
24. C. Manzo, M. F. Garcia-Parajo, *Rep. Prog. Phys.* **78**, 124601 (2015).
25. S. Scott *et al*., *Phys. Chem. Chem. Phys.* **25**, 1513–1537 (2023).
26. W. W. Ahmed *et al*., *Biophys. J.* **114**, 1667–1679 (2018).
27. S. Salinas-Almaguer *et al*., *Sci. Rep.* **12**, 933 (2022).
28. R. Garcia-Millan, G. Pruessner, *J. Stat. Mech.* **2021**, 063203 (2021).
29. H. Turlier, T. Betz, *Annu. Rev. Condens. Matter Phys.* **10**, 213–232 (2019).
30. Y.-Z. Yoon *et al*., *Biophys. J.* **97**, 1606–1615 (2009).
31. T. Betz, M. Lenz, J.-F. Joanny, C. Sykes, *Proc. Natl. Acad. Sci. U.S.A.* **106**, 15320–15325 (2009).
32. T. J. Byers, D. Branton, *Proc. Natl. Acad. Sci. U.S.A.* **82**, 6153–6157 (1985).
33. M. Mell, F. Monroy, *PLOS ONE* **13**, e0207376 (2018).
34. P. Martin, A. J. Hudspeth, *Proc. Natl. Acad. Sci. U.S.A.* **96**, 14306–14311 (1999).
35. G. Tucci *et al*., *Phys. Rev. Lett.* **129**, 030603 (2022).
36. D. E. Discher, N. Mohandas, E. A. Evans, *Science* **266**, 1032–1035 (1994).
37. C. Nardini *et al*., *Phys. Rev. X* **7**, 021007 (2017).
38. T. GrandPre, K. Klymko, K. K. Mandadapu, D. T. Limmer, *Phys. Rev. E* **103**, 012613 (2021).
39. T. Markovich, É. Fodor, E. Tjhung, M. E. Cates, *Phys. Rev. X* **11**, 021057 (2021).
40. U. Bandmann, M. Monti, I. Wadsö, *Scand. J. Clin. Lab. Invest.* **35**, 121–127 (1975).
41. P. Bäckman, *Thermochim. Acta* **205**, 87–97 (1992).
42. E. Ben-Isaac *et al*., *Phys. Rev. Lett.* **106**, 238103 (2011).
43. D. M. Busiello, S. Pigolotti, *Phys. Rev. E* **100**, 060102 (2019).
44. D.-K. Kim, Y. Bae, S. Lee, H. Jeong, *Phys. Rev. Lett.* **125**, 140604 (2020).
45. P. Bilotto, L. Caprini, A. Vulpiani, *Phys. Rev. E* **104**, 024140 (2021).
46. A. I. Brown, D. A. Sivak, *Chem. Rev.* **120**, 434–459 (2020).
47. N. V. Dokholyan, *Chem. Rev.* **116**, 6463–6487 (2016).
48. A. Wachtel, R. Rao, M. Esposito, *J. Chem. Phys.* **157**, 024109 (2022).
49. K. S. Peters, G. J. Snyder, *Science* **241**, 1053–1057 (1988).
50. C. Riedel *et al*., *Nature* **517**, 227–230 (2015).
51. I. Di Terlizzi *et al*., Variance sum rule for entropy production. (2023); https://doi.org/10.5061/dryad.h44j0zpsw

ACKNOWLEDGMENTS

Funding: M.G. and F.R. are supported by the Spanish Research Council (grant PID2019-111148GB-100 and PID2022-139913NB-100). D.H.-A. and F.M. are supported by the Spanish Research Council (grant PID2019-108391RB-100 and grant TED2021-132296B). T.B. is supported by the European Research Council (consolidator grant 771201 and the Deutsche Forschungsgemeinschaft under Germany's Excellence Strategy - EXC 2067/1-390729940). M.B. is supported by research grant BAIE_BIRD2021_01 from the University of Padova. F.R. is supported by ICREA Academia 2018. **Author contributions:** I.D.T., M.B., and F.R. conceptualized the study; M.G., D.H.-A., T.B., and F.M. collected and curated the data. I.D.T. wrote the software for data analysis and performed visualization. I.D.T. and M.G. analyzed the data. F.R. administered the project. I.D.T., M.B., and F.R. wrote the original draft. All authors discussed the results and implications of the methodology and commented on the manuscript. **Competing interests:** The authors declare no competing financial interests. **Data and materials availability:** All data needed to evaluate the conclusions in the paper, and the code for fitting the VSR, are available at Dryad (*51*). Figures 1A and 2A, fig. S1, and the inset of Fig. 3A were created with BioRender.com.

SUPPLEMENTARY MATERIALS

science.org/doi/10.1126/science.adh1823
Materials and Methods
Supplementary Text
Figs. S1 to S15
Tables S1 to S5
References (*52*–*60*)

Submitted 16 February 2023; accepted 9 January 2024
10.1126/science.adh1823